

On the prospect of discovering ‘galaxy groups’ through radio observations

SURAJIT PAUL,¹ PRATEEK GUPTA,¹ REJU SAM JOHN,^{2,1} AND VENKAT PUNJABI¹

¹*Department of Physics,
SP Pune University, Pune 411007, India*

²*Department of Physics, Pondicherry Engineering College,
Puducherry, 605014, India*

Submitted to ApJ

ABSTRACT

Observed steep mass scaling of radio power from the available high mass galaxy clusters has ruled out the prospect of detection of ‘galaxy groups’. On the other hand, the available simulations and observations of thermal emissions show that the groups are merger prone, thus non-virialised, indicating better visibility in the non-thermal radio waves. Detection of radio emissions from them would help us to understand the scale-dependent effectiveness of particle acceleration mechanisms, as well as, being younger and cooler than clusters, groups can be a unique laboratory to test the models of cosmic magnetism. They can also be the potential source of Warm-Hot Intergalactic Medium (WHIM). So, in this study, we have modelled radio emissions from the structures in cosmological hydrodynamic simulations performed using ENZO. We present a simple model for computing magnetic field using turbulence and for the first time, used the electron energy spectrum from both the diffusive shock acceleration (DSA) and turbulent re-acceleration (TRA) mechanisms to compute radio synchrotron emissions. Computed radio power from a wide range of mass ($\geq 10^{13}$ to $2 \times 10^{15} M_{\odot}$) with a sample of more than 200 simulated objects show a new mass scaling of $M_{500} \propto P_{1.4 \text{ GHz}}^{2.17 \pm 0.08}$ and a strong correlation scale of $L_X \propto P_{1.4 \text{ GHz}}^{1.08 \pm 0.05}$. Both magnetic field and radio power are shown to have adequately replicated the available observations at high mass, allowing us to extend the results to further smaller masses. We report that groups below $10^{14} M_{\odot}$ show the existence of 10s of nano-Gauss to a sub- μG magnetic field and about $10^{19-23} \text{ W Hz}^{-1}$ of radio power, much higher than what existing mass scaling predicts. We found that the combined radio power from TRA and DSA electrons can only fit very well to all the observed ‘radio halos’ which significantly improves our understanding about radio halo emission. Finally, we have implemented this model on a real data set obtained from the Sloan Digital Sky Survey (SDSS). It predicts about 10s to 100s $\mu\text{Jy}/(10'' \text{ beam})$ of radio flux in groups indicating their detectability with existing and aplenty with the future radio telescopes.

Keywords: editorials, notices — miscellaneous — catalogs — surveys

1. INTRODUCTION

The large scale matter distribution in the universe has an interconnected web like structure that is comprising of galaxies, galaxy groups, large filaments and clusters of galaxies (Jones et al. 2004; Springel et al. 2006). In the structural hierarchy, ‘galaxy groups’ (for definition see Paul et al. (2017))

are the intermediate objects between the field galaxies and the rich galaxy clusters (Freeland & Wilcots 2011). Groups, that usually form inside the dark matter (DM) filaments connecting the clusters (Lietzen et al. 2012; Tempel et al. 2014a; Vajgel et al. 2014), appear like series of knots on a long string (Tempel et al. 2014a) and eventually pulled towards the nodes (clusters) (Pimbblet 2011; Perez et al. 2009; Moss 2006). They are thus observed to be stretched along the filaments (Zhang et al. 2013), possibly due to their rapid movement towards the cluster. While moving through these DM channels, they would experience tremendous shear force and dynamical friction and get squeezed along the perpendicu-

Corresponding author: Surajit Paul
surajit@physics.unipune.ac.in, surajit@associates.iucaa.in

Corresponding author: Prateek Gupta
prateek@physics.unipune.ac.in

lar direction to the filaments, increasing the rate of collisions among the constituent galaxies (Struck 2011; Diaferio et al. 1993; O’Sullivan et al. 2015).

Groups are mostly found to be non-virialized because, they are very much unstable to mergers as shown in N-body simulations (Carnevali et al. (1981); Diaferio et al. (1993)), in recent work by Díaz-Giménez & Mamon (2010), and in hydrodynamical simulations by Paul et al. (2017). Moreover, being inside the shallower gravitational potential of filaments, they are expected to be more strongly affected by processes such as mergers, feedback from super-massive black holes (SMBH), and galactic winds etc. (Lovisari et al. 2015). Fractional cosmic ray content that mainly depends on Mach number of shocks in the inter-galactic medium (IGM) is also reported to be larger in some galaxy groups compared to the clusters (Jubelgas et al. 2008; John et al. 2018). In a recent work by Paul et al. (2017), it has been shown that the CR luminosity follows a different evolutionary path than that of the clusters and fluctuations of CR luminosity in low mass systems observed to be higher in their merging state (John et al. 2018). The frequent merger would introduce turbulence and may allow groups to re-accelerate particles and convert more thermal energy to non-thermal energy. This indicates that non-thermal scaling laws derived from the cluster observations may not be obeyed by the groups. In fact, such deviation has also been reported by Paul et al. (2017). So, the study of galaxy groups can provide vital information of an intermediate environment between the field galaxies and the clusters (Berrier et al. 2009), especially in non-thermal emissions.

In recent years, the importance of low mass objects in understanding large scale structure (LSS) formation and its energy evolution has been pointed out by various researchers (Paul et al. 2017; Bharadwaj et al. 2015; Vajgel et al. 2014; Pratt et al. 2009). But, their non-thermal properties, especially the radio emissions remained almost unexplored. Since, non-thermal radiations depend more on the transient activities such as mergers, shocks, and turbulence etc., it can reveal much more information about the dynamics of LSS (for review Dolag et al. (2008); Brüggén et al. (2012)) over any other form of energies. But, groups are not sufficiently observed yet in non-thermal emissions and no general properties are studied in this regard. Cluster mass-scaling with existing radio observations (Cassano et al. 2013; Yuan et al. 2015) indicate a steep slope of about 4, removing the possibility of detection of galaxy groups (mass $< 10^{14} M_{\odot}$) with currently available telescope facilities. But, as the data available or used in these studies are incomplete (only for massive clusters $\gtrsim 5 \times 10^{14} M_{\odot}$), it may not be very wise to extrapolate this to a wide range of masses. Paul et al. (2017) shows, turbulence and cosmic rays from group significantly deviates from cluster scaling and becomes flatter, indicating

better visibility of groups through their non-thermal properties. This motivated us to model the radio emissions from smaller objects through simulations.

In this study, we have performed cosmological hydrodynamic plus N-body simulations using Enzo code (Bryan et al. 2014) with a specific aim to understand the non-thermal radio emissions from objects at different scales ranging more than two orders of magnitude in mass ($10^{13} M_{\odot} - 10^{15} M_{\odot}$). We have theoretically modelled LSS taking into account of radiative cooling, heating due to star motions and supernova and star formation feedback physics. AGN feedback may have a non-negligible effect in the core of very low mass ($\sim 10^{13} M_{\odot}$) systems (McCarthy et al. 2010), but this is out of scope of this work and thus becomes a topic for future study (see details of our used model in Paul et al. (2017)). Using the above model, we have created a mock sample of more than 200 objects for our study. We have the smaller clusters and galaxy groups in plenty that are not yet explored well in radio waves, leaving a vacuum of information in between field galaxies and the clusters. The wide range of mass in our study helped us to compare our simulated objects with the available observations and to constrain our model which in turn, made us able to extrapolate our results to the smaller objects more accurately. Further, our model has been applied to compute possible radio emissions from real objects in the SDSS galaxy group list (Tempel et al. 2014b). Finally, we have computed possible observable fraction of these SDSS group sample for the available and upcoming highly sensitive radio telescopes such as uGMRT, SKA and so on.

This article has five sections. After giving an introduction in Section 1, we have described our simulation details and mentioned about computed and observed data samples in Section 2. Our model of finding turbulence, computing magnetic fields and radio emissions from different particle acceleration mechanisms are described in Section 3. We have discussed our simulation results and implementation of our model on the observed SDSS sources with the possibility of observations in Section 4. Finally, results have been summarised and concluded in the Section 5.

2. DATA SELECTION DETAILS

2.1. Simulation details and the data

To understand and make a possible theoretical estimation of non-thermal radio emission from groups, we have created our sample of objects by performing simulations with the adaptive mesh refinement (AMR), grid-based hybrid (N-body plus hydro-dynamical) code Enzo v. 2.2 (Bryan et al. 2014; O’Shea et al. 2004). A $(128 \text{ Mpc})^3$ volume has been simulated with the introduction of 2 nested child grid and further 4 levels of AMR at the central $(32 \text{ Mpc})^3$ volume, a resolution of about 30 kpc has been achieved at the highest resolved level. As cosmological parameters, we have taken

a flat Λ CDM background cosmology with $\Omega_\Lambda = 0.7257$, Ω_m now = 0.2743, $\Omega_b = 0.0458$, $h = 0.702$ and primordial power spectrum normalization $\sigma_8 = 0.812$ (Komatsu et al. 2009).

Since, shocks and turbulence are the two most important parameters that are required to compute radio emissions (Further details in Section 3), we paid more attention to these parameters in our simulations. The shocks have been computed in our simulations using un-split velocity jump method of Skillman et al. (2008) with a temperature floor of $T^4\text{K}$. This method is found to produce better results in AMR simulations (Vazza et al. 2011). Since shocks are very much important mainly for DSA computation, in our adaptive mesh refinement strategy, the refinement criteria based on shocks along with the over-density (both in DM and baryon) have been used. A detailed account of the AMR criteria used here can be found in John et al. (2018). Turbulence, on the other hand, is a derivative of kinetic energy due to dynamics of the systems which is in turn controlled by the distribution of different forms of energies in the inter cluster and inter galactic medium. So, to obtain a more realistic energy distribution in the LSS, a formulation has been used that includes the effect of radiative cooling due to X-ray, UV & optical emissions and heating due to stellar motions and Supernova (Sarazin & White 1987). We have also used the star formation and feedback scheme of Cen & Ostriker (1992) with a feedback of 0.25 solar in our simulations. In short, we call this model with additional physics as ‘coolSF’ runs (for details, see Paul et al. (2017)).

With the above-said model, we have simulated 10 realizations of $(128 \text{ Mpc})^3$ volume. We have used the 30 kpc resolution simulations as the reference set (‘REFRES’ hereafter). Each simulation has been started at redshift $z=60$ and ran till $z=0$. We have taken several snapshots at different redshifts, mostly at the low redshift (below $z=1$). Further, computations of different physical properties for this study have been performed as the post processing of these simulated snapshots by using the yt-tools (Turk et al. 2011).

2.1.1. Simulated data set

From one of our simulations, a slice of $(30 \text{ Mpc})^2$ area has been plotted in Figure 1. It shows a filamentary structure around few massive clusters shown as bigger white circles. Smaller circles representing groups and are observed to be in abundant numbers and placed mostly along the filaments in accordance with the observations as discussed in section 1.

We have identified groups and clusters from our simulations using the HOP algorithm (Eisenstein & Hut 1998) implemented in yt (Turk et al. 2011). The initial sample was selected depending on their M_{500} mass. Where M_{500} is the mass within the radial distance where over-density of the objects become 500 times the critical density of the universe at that redshift. In this scale, usually ‘virial radius’ refers to

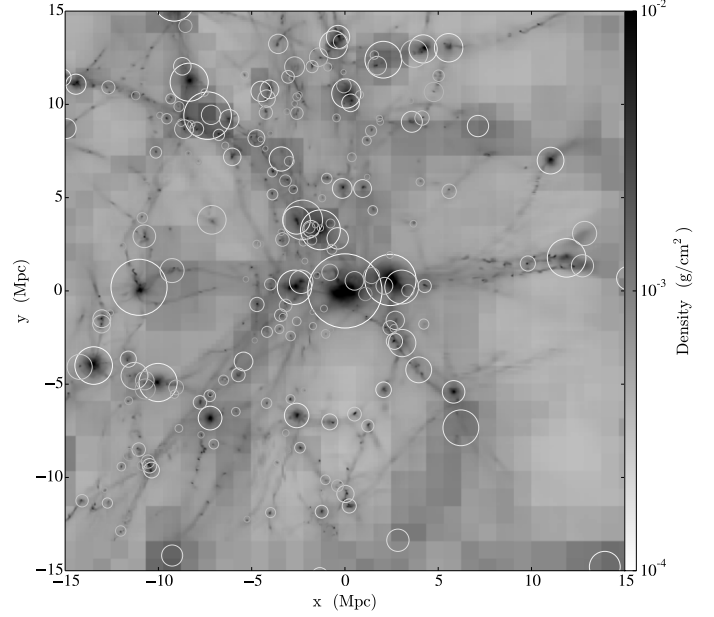


Figure 1. Baryon density plotted for $(30 \text{ Mpc})^2$ simulated area. White circles indicate the structures and circle radius is same as their virial radius i.e. r_{200} .

the radius at over density of 200. Each of our $(128 \text{ Mpc})^3$ volume simulations were focused on a central cluster, but, a large number of other objects are available within the $(32 \text{ Mpc})^3$ central high resolution volume where AMR has been allowed. So, adding to the main 10 clusters, we have a few hundreds of objects with the same resolution when we considered the data from different sets of simulations and from different snapshot outputs. To make sure that the DM particles and baryon gas that forms these objects of interest are mostly coming from the well refined Lagrangian region, we have taken the objects only within central $(20 \text{ Mpc})^3$ volume. Finally, we have chosen over 200 groups and clusters with masses above $10^{13} M_\odot$ and it spans till $2 \times 10^{15} M_\odot$. Our mass resolution at the smallest child grid is $< 10^9 M_\odot$ providing enough mass resolution for the groups with at least 10^4 particles. Also, with ~ 30 kpc spatial resolution, systems above $10^{13} M_\odot$ at r_{500} that have virial radii above 500 kpc provide adequate spatial resolution with at least 1000s of cells.

2.2. Observed data set from SDSS group catalogue

Along with the simulated data, we have chosen a set of observed data from Sloan Digital Sky Survey (SDSS). Model devised through simulations has been implemented to this data set to make an estimation of expected radio flux from real objects. Our primary observed data source is the ‘galaxy group’ catalogue of Tempel et al. (2014b) prepared using the SDSS, Data Release-10. On the tabulated galaxy data, au-

thors applied Friends of Friends (FoF) algorithm, and identified a total of 82,458 galaxy groups by defining groups as an object having at least 2 galaxies and choosing suitable linking length (see Tempel et al. (2014b) for details). We know that a group of galaxies is a gravitationally bound system with a mass of approximately $10^{13} M_{\odot}$ and with a radius of just less than a Mpc and temperature $\lesssim 1$ keV (Paul et al. 2017). So, to ensure the group properties, we have chosen only those objects that are having at least 10 numbers of galaxy candidates and having total mass greater than $10^{13} M_{\odot}$ to remove the possibility that groups properties get dominated by merely a few galaxies. We have only put constraint on minimum mass and kept all the higher mass objects (clusters) in the list to compare them with the available observations as well as simulations. So, in our sample, we got 2300 objects with masses in the range of $10^{13} - 2 \times 10^{15} M_{\odot}$, the same range as the simulated sample set that we are working with.

3. MODELLING RADIO SYNCHROTRON EMISSION FROM GROUPS AND CLUSTERS

Radio synchrotron emission strongly depends on the energy distribution of available charged particles in astrophysical plasma as well as the magnetic field in the medium (Feretti & Giovannini 2008; Rephaeli & Persic 2015; Kale et al. 2016). The power spectrum of radio emission is determined by the energy spectrum of the radio emitting electrons which is determined by the particle acceleration mechanisms active in these objects. In large scale astrophysical systems, the known major particle acceleration mechanisms are Diffusive Shock Acceleration (DSA) i.e. Fermi I (Drury 1983) and Turbulent Re-acceleration (TRA) i.e. Fermi II (Brunetti & Lazarian 2007) mechanism). Shocks and turbulence in the IGM are also very important as they determine the strength of magnetic fields either by amplification by compression (Iapichino & Brüggén 2012) or by the turbulent dynamo (Subramanian et al. 2006).

3.1. Shocks and turbulence in groups and clusters

3.1.1. Shocks in groups and clusters

Structure mergers can release binding energy of about 10^{61} ergs (groups of mass of $10^{13} M_{\odot}$) to 10^{65} ergs (clusters of mass of $10^{15} M_{\odot}$). It has been proposed that the energy released during these mergers create huge pressure in the core of the objects and the medium eventually starts expanding supersonically like a blast wave, inducing strong shocks in the baryonic gas (Ha et al. 2017; Paul 2012; Sarazin 2002) and travels radially as spheroidal wave-front towards the virial radius and moves beyond (van Weeren et al. 2011; Machado & Lima Neto 2013; Ha et al. 2017; Paul et al. 2011; Iapichino et al. 2017). Shocks then dissipate energy through heating and turbulence stirring in the medium (Sarazin & White 1987; Dolag et al. 2005; Paul et al. 2011). Also, due to shock

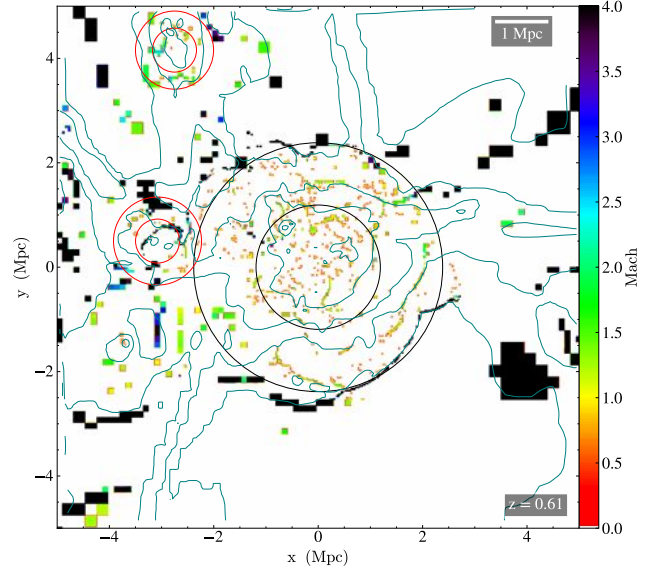


Figure 2. Mach number of shocks has been plotted as colour map. Black circles are showing the r_{1000} (inner) and r_{200} (outer) of a big cluster. Same for the groups are shown as red circles.

acceleration, charged particles in the thermal plasma gets accelerated to high energies. Time-scale of such dissipation for a single merger is found to be about 1-2 Gyr (Paul et al. 2011; Roettiger et al. 1999) indicating an energy dissipation rate of the order of $10^{47} \text{ erg s}^{-1}$ (John et al. 2018). If a few percent of this energy goes to radio emissions, it amounts to at least about $10^{45} \text{ erg s}^{-1}$.

In our simulated objects (Fig. 2 is shown as a representative map), in general it is found that in the clusters (indicated by large black circles), shock Mach numbers varying in the range $\mathcal{M} = 1 - 2$ in the core region i.e. inner circle at r_{1000} . It goes to almost $\mathcal{M} = 4$ in regions beyond the core but inside virial radius i.e. outer circle at r_{200} , it rarely reaches as high as $\mathcal{M} = 10$. These are usually known as the merger or the internal shocks (Miniati et al. 2000; Skillman et al. 2008). Outside the virial radius (i.e. r_{200}), it goes beyond $\mathcal{M} = 10$ due to continuous accretion of matter known as accretion or external shocks. Whereas, in the groups, depicted as smaller concentric red circles, we hardly see any shocks inside r_{1000} i.e. inner circle.

3.1.2. Turbulence in groups and clusters

Galaxy groups while flowing along the filaments, shown to inject high level of vorticity ($\omega = \nabla \times v$) (see Fig. 3, Panel 1). It can be noticed that while the clusters are having the highest level of vorticity magnitude about $5 \times 10^{-16} \text{ s}^{-1}$, groups are not far behind. The yellow-green patches along the filaments in Fig 3 Panel 1, are the groups (marked with smaller red circles) and are having vorticity varying in the range of

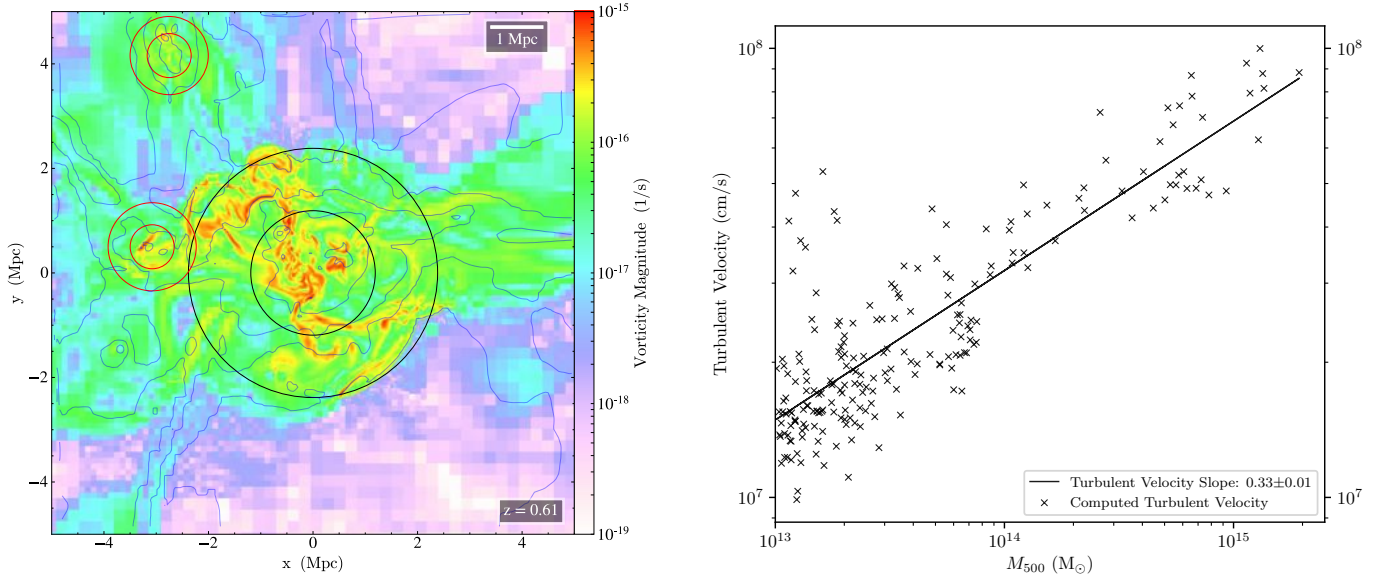


Figure 3. Panel 1: 20 Mpc² simulated area with vorticity in colour. Circles are representing clusters and groups similar to Figure 3.1.1. **Panel 2:** Velocity dispersion of baryons with the mass (M_{500}) of the objects from our simulated data set.

few times 10^{-17} to even $3 \times 10^{-16} \text{ s}^{-1}$, values not very far compared to the clusters.

Turbulent energy in cluster medium is dominated by ($\sim 90\text{--}95\%$) the solenoidal mode which comes from the rotational motions in the IGM (Miniati & Beresnyak 2015; Vazza et al. 2017). So, a fluid with non-zero vorticity $\vec{\omega} = \nabla \times \vec{v}$ will have non zero values of turbulent energy. The direction of $\vec{\omega}$ being random, vectorial average tends to be zero. Therefore the magnitude of vorticity is an important factor for calculation of turbulent energy. Enstrophy, given by $\xi = \int_S \omega^2 dS$. ξ , which is an integral of square of vorticity over a surface S , is a proxy to the dissipation of kinetic energy to turbulent energy (Zhu & Antonia 1997; Vazza et al. 2017; Iapichino et al. 2010). So, it can be related to the turbulent flow by the Kinetic energy content per unit mass $\epsilon_{\text{turb}} \approx 1/2(v_{\text{rms}}^2)$, where v_{rms} i.e. velocity dispersion of the medium. This tells us that the quantification of local velocity dispersion i.e. root mean square velocity (v_{rms}) would suffice to estimate turbulent energy.

In this study, v_{rms} has been computed by filtering out the bulk motions of baryons in the core (r_{1000}) of the groups from our simulated objects (also see Paul et al. (2015)). Finally, this allowed us to compute the turbulent energy of the dominant solenoidal flow mode. A volume weighted spherically averaged quantity within r_{500} is computed to get the average turbulent energy from each object. With this simple method of computing the local turbulent velocity, we got average values of about 100 to 300 km s⁻¹ in our simulated groups (up to the mass $10^{14} M_{\odot}$) that corroborates the observed values well (Rasmussen et al. 2006; Wilman et al. 2005; Tully 1987).

But, a noticeable fraction of the groups are found to be very active with even much higher values of turbulence at 300-600 km s⁻¹, almost at the level of clusters (mass beyond $10^{14} M_{\odot}$) which shows values varying in the range 300-1000 km s⁻¹ (Fig. 3, Panel 2). This is very much in accordance with our expectations (see Section 1).

3.2. Computing magnetic field

Turbulent energy increases the particle energy stochastically (Brunetti & Lazarian 2007; Donnert & Brunetti 2014) or gets converted to magnetic energy through turbulent dynamos (Subramanian et al. 2006; Rincon et al. 2016). It has been reported that magnetic field of μG that we usually observe today (Govoni & Feretti 2004) in the inter cluster medium (ICM), can be achieved through this turbulent dynamos (Xu et al. 2009; Ryu et al. 2008). This mechanism can boost the level of IGM seed magnetisation of about 10^{-21} Gauss at re-ionisation era to the present value of μG . Such kind of amplification of magnetic field certainly needs a very high degree of turbulence in the medium i.e. a fully developed or Kolmogorov type, $E(k) \propto k^{-5/3}$ (Egan et al. 2016). A quasi-equipartition is reached between magnetic energy density $\frac{B^2}{8\pi}$ and the kinetic energy density $\rho\epsilon_{\text{turb}}$ in such a fully turbulent medium (Miniati & Beresnyak 2015). So, the saturated magnetic field can easily be obtained from the available hydrodynamic parameters in our simulations by the below given relation

$$\frac{B_{\text{sat}}^2}{8\pi} \propto \rho\epsilon_{\text{turb}} \text{ i.e. } B_{\text{sat}} = \sqrt{C_E \cdot 8\pi \cdot \rho\epsilon_{\text{turb}}} \quad (1)$$

(Subramanian 1998; Iapichino & Brüggén 2012) where, ϵ_{turb} is the local turbulent energy which is a fraction of the kinetic energy of the medium. The constant of proportionality C_E can be at the max 0.05 (Miniati & Beresnyak 2015).

3.3. Computing synchrotron radio emissions

3.3.1. Radio emission due to DSA

The ICM and IGM are shocked due to mergers or accretion of mass clumps during large scale structure formation (see section 3.1.1). Shocks in the clusters, thermalizes the ICM to as high as $10^{7-8} K$. Calculation using Saha-ionisation equation (Saha 1920) shows this medium to be fully ionised. These highly energetic thermal electrons then pumped into the shocks. Injected charge particles gain energy and get accelerated by crossing these shocks multiple times (Fermi-I mechanism or DSA) and produce a power law energy spectrum with relativistic energy given by $n(E)dE \propto E^{-\delta}dE$ (Drury 1983; Baring & Summerlin 2009), where δ is the spectral index which is related to the density compression ratio, C , as $\delta = (C + 2)/(C - 1)$ (Hoeft & Brüggén 2007) where density compression ratio can be obtained by Mach number (M) of the shocks as $C = 4M^2/(M^2 + 3/2)$ (Drury 1983) with polytropic index $\gamma = 5/3$. So, final spectral index is a strong function of shock Mach number. These electrons then gyrate in the magnetic field compressed by these shocks or amplified by the turbulence and eventually radiates synchrotron radio emission from the shock surfaces. In this respect a well used relation for radio power due to DSA electron has been derived by Hoeft & Brüggén (2007)

$$\frac{dP(\nu_{\text{obs}})}{d\nu} = 6.4 \times 10^{34} \frac{\text{erg}}{\text{sHz}} \left(\frac{A}{Mpc^2} \right) \left(\frac{n_e}{10^{-4} \text{cm}^{-3}} \right) \left(\frac{T}{7 \text{keV}} \right)^{\frac{3}{2}} \times \left(\frac{\xi_e}{0.05} \right) \left(\frac{\nu_{\text{obs}}}{1.4 \text{GHz}} \right)^{-\frac{\delta}{2}} \frac{\left(\frac{B}{\mu G} \right)^{1+\frac{\delta}{2}}}{\left(\frac{B_{\text{CMB}}}{\mu G} \right)^2 + \left(\frac{B}{\mu G} \right)^2} \Psi(M) \quad (2)$$

where A is the area of the shock wave, B is magnetic field, B_{CMB} is the magnetic field corresponding to the energy density of Cosmic Microwave Background Radiation (CMBR), ξ_e is the electron acceleration efficiency, ν_{obs} is the observed frequency, n_e is the post-shock electron density, and T is post-shock temperature. $\Psi(M)$ is a dimensionless function of shock Mach number. For strong shocks ($M \geq 5$), it saturates to $\Psi \sim 1$, while for weak shocks ($M \leq 3$), Ψ function dies out rapidly (Hoeft & Brüggén 2007).

In our simulations, we have obtained the post-shock temperature and computed the Mach number of the shocked cells using the unsplit velocity jump as described by Skillman et al. (2008). Post-shock electron density is being computed on each cell as post process derived quantities. Shocked surface area has been approximated here as the sum of the area of one surface of each of the cells tagged as shocked (See

Vazza et al. (2017)). Computation of radio power through DSA is being done on each cell in shocked regions with having Mach number greater than $M=1.5$ as the radio emission shown to take place only beyond Mach $M=1.5$. It has also been noticed that power emitted by shocks rapidly falls beyond Mach $M=4.5$ (Hong et al. 2014). The Mach number range of $M=1.5-4.5$ is also found to be the most effective cosmic ray producer (John et al. 2018), indicating more availability of synchrotron electrons.

3.3.2. Radio emission due to TRA

Turbulence generated in forming structures (mainly during mergers) as discussed in section 3.1.2 can re-accelerate ambient energetic charge particles stochastically by the process known as the Fermi II or the Turbulent Re-Acceleration (TRA) (Brunetti et al. 2001; Brunetti & Lazarian 2007). Induced turbulence in the IGM generates Alfvén waves through Lighthill radiation (Lighthill 1952). These Alfvén waves accelerate ambient high energy electrons to GeV energies. The highest energy electrons those could resonate with the turbulence is given by (Fang & Linden 2016) as;

$$E_{\text{max}} = 53 \text{GeV} \left(\frac{B}{\mu G} \right)^{\frac{4}{3}} \left(\frac{T}{2 \text{keV}} \right)^{-\frac{1}{6}} \left(\frac{l_0}{300 \text{kpc}} \right)^{\frac{2}{3}} \times \left(\frac{v_t}{300 \text{km s}^{-1}} \right)^{-\frac{4}{3}} \left(\frac{n_e}{10^{-3} \text{cm}^{-3}} \right)^{-\frac{1}{6}} \quad (3)$$

v_t is the turbulent velocity which we have computed as discussed in section 3.1.2 and l_0 is the largest eddy size of the system (or the largest turbulent scale in the system) which can be defined as $l_0 = V_T \tau_0$, where V_T is the velocity difference of largest eddy scale and τ_0 is the Hubble time (Stein 1974). As a first order approximation, we have used the most probable velocity within the individual groups and clusters as the value for V_T . Usually, turbulence life time in the groups and clusters are not the Hubble time, rather it is the time of sustenance of the turbulence in the system after has been induced by the mergers. We have thus taken τ_0 to be about 2 Gyr as reported by (Paul et al. 2011). This gives us well comparable largest eddy scales as estimated by Subramanian et al. (2006); Goldman (1998).

In TRA, the particle energy spectrum takes up the form

$$\left(\frac{dn_e}{dE_e} \right) = \frac{3P_A c}{4S(E_{\text{max}})^{1/2}} E_e^{-\delta} \quad (4)$$

(Fang & Linden 2016), where, P_A is the part of the total turbulent power going into the Alfvén waves and is given by

$$P_A = 4.2 \times 10^{-32} \text{erg cm}^{-3} \text{s}^{-1} \left(\frac{v_t}{300 \text{km s}^{-1}} \right)^{\frac{23}{6}} \left(\frac{B}{\mu G} \right)^{-\frac{4}{3}} \times \left(\frac{T}{2 \text{keV}} \right)^{-\frac{1}{12}} \left(\frac{n_e}{10^{-3} \text{cm}^{-3}} \right)^{\frac{5}{3}} \left(\frac{l_0}{300 \text{kpc}} \right)^{-\frac{7}{6}} \quad (5)$$

and $\delta = \frac{5}{2}$ with an assumption of Kolmogorov type i.e. fully developed turbulence, and

$$S = \frac{4(B^2 + B_{CMB}^2)e^4}{9m_e^4c^6} \quad (6)$$

where $S p^2 c$ corresponds to the synchrotron and inverse Compton emission power of an electron (Fang & Linden 2016). Using the above particles energy spectrum, the radio synchrotron power through turbulent re-acceleration mechanism computed as

$$\frac{d^2 P(\nu_{obs})}{dV d\nu} = \frac{\sqrt{3}e^3 B}{8m_e c^2} \int_{E_{min}}^{E_{max}} dE_e F\left(\frac{\nu_{obs}}{\nu_c}\right) \left(\frac{dn_e}{dE_e}\right)_{inj} \quad (7)$$

where, ν_c is the critical frequency of synchrotron emission,

$$\nu_c = \frac{3\gamma^2 e B}{4\pi m_e} = 0.016 \left(\frac{B}{1\mu G}\right) \left(\frac{E_e}{1GeV}\right)^2 \text{ GHz} \quad (8)$$

and

$$F(x) = x \int_x^\infty K_{5/3}(x') dx' \quad (9)$$

is the synchrotron emission function, which peaks at $x = 0.29$, $K_{5/3}$ is the modified Bessel function of order 5/3 (Longair 2011).

4. RESULTS AND DISCUSSIONS

4.1. Computed magnetic fields

We have implemented the model described in section 3.2 on a Coma-like cluster with similar mass, radius (about M_{200} about $10^{15} M_\odot$, r_{200} about 3 Mpc; within the error bars of Kubo et al. (2007); Brilenkov et al. (2015)) and dynamical state (relatively relaxed (Kent & Gunn 1982), with presence of a few sub-clumps) in our simulation. Our modelled magnetic field is in good agreement with the radial profile of Coma cluster plotted till r_{500} using Faraday rotation measurements (Bonafede et al. 2010) (see Fig. 4, Panel 1). Further, using the same model, we have computed the magnetic fields for all the objects in our sample used for this study and found average magnetic field $\langle B \rangle$ of about μG from the core (r_{1000}) of the clusters (above $5 \times 10^{14} M_\odot$) as expected from many Faraday rotation observations of galaxy clusters (Eilek & Owen 2002; Govoni & Feretti 2004). Whereas, groups are found to have 10s of nano-Gauss to sub μG magnetic field with a considerable amount of fluctuations in their values (see Fig. 4, Panel 2).

4.2. Modelled radio emissions

Our radio emission models described in section 3.3.1 and section 3.3.2 have been implemented to compute 1.4 GHz radio synchrotron emission power from both DSA and TRA

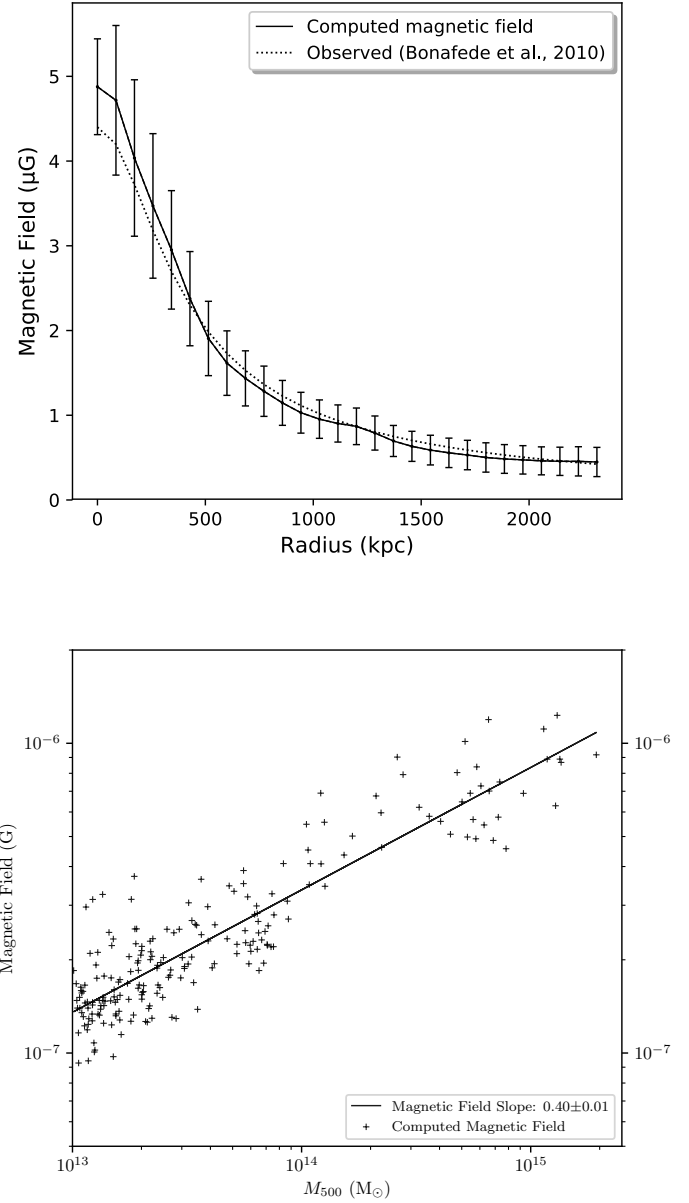


Figure 4. Panel 1: Computed radial magnetic field over-plotted on observed Coma cluster magnetic field. **Panel 2:** Computed magnetic field for the selected samples plotted against the mass (M_{500}).

electrons in the chosen simulated objects. From an observational point of view, we have also performed a band integration over the central frequency 1.4 GHz with the band size of 32 MHz (e.g. GMRT L band) to compute radio synchrotron power from both DSA and TRA mechanisms. The magnetic fields computed using the formulation described in section 3.2 are used in these calculations. To verify and constraint our model from observations, we need to understand the bulk properties of the sources for which adequate

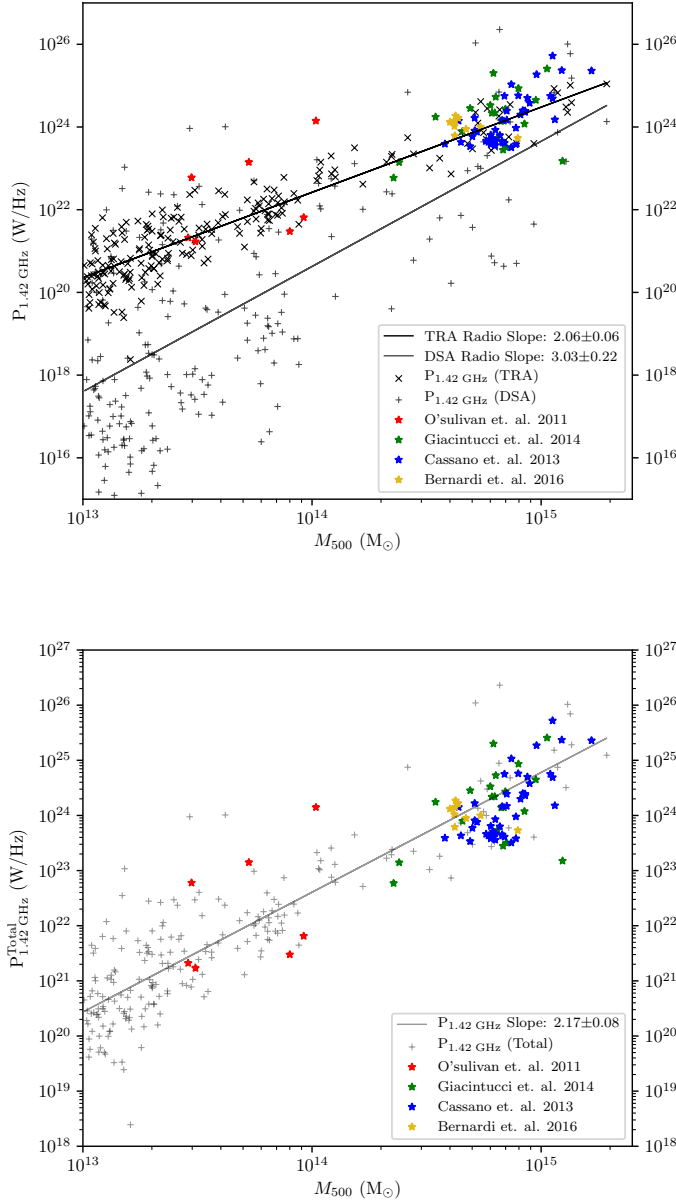


Figure 5. Panel 1 Over-plotted observation data on modelled radio power from DSA & TRA models from simulated groups and clusters. **Panel 2** Same set of observed data has been plotted over the computed total radio power.

observations are available. Since, radio halos have been studied adequately, at least at large masses, we have computed mainly the halo emissions for the comparison. Radio halo emission in the clusters are usually found to be of sizes about a Mpc (Feretti & Giovannini 2008; Giovannini et al. 2009; Paul et al. 2014) in the core region i.e. their linear extension can be well approximated to their r_{1000} radius. So, we compute the radio emissions from this region only. As we have

seen in the section 2 that shocks are also present in plenty inside the core, we understood that while computing the radio halo emission from cluster cores, the emission due to DSA cannot be neglected.

Results show that the radio power of the sources vary from $10^{15} \text{ Watt Hz}^{-1}$ to $10^{26} \text{ Watt Hz}^{-1}$ with different mass scaling for DSA and TRA. We have over-plotted observed data of radio power at 1.4 GHz from Bernardi et al. (2016); Giacintucci et al. (2014); Cassano et al. (2013, 2007); O'Sullivan et al. (2011) on our modelled radio power plot. It has been noticed that for many objects, radio emissions due to DSA electrons are equally important as the TRA for emissions from the central halo (within R_{1000}), especially from the objects with mass greater than $10^{14} M_{\odot}$. While, in lower mass systems, TRA turns out to be more effective (see Fig. 5, Panel 1). From the observations, we have very few points below mass of $5 \times 10^{14} M_{\odot}$ and the plotted few red and green points were thought to be outliers (Giovannini et al. 2011), considering the scaling laws of clusters beyond $5 \times 10^{14} M_{\odot}$ as the reference which follow a much steeper mass scaling of about 4 (Cassano et al. 2013; Yuan et al. 2015). But, when we add up the radio powers from DSA and TRA and over-plotted again the observed data, the thought outliers perfectly fell along the same line indicating a possible misinterpretation by an incomplete and subset of observed data (above $5 \times 10^{14} M_{\odot}$) in the literature and thus validates our theoretical model and allowed us to extend it to the lower mass objects as well. Here we report a new predicted correlation of $M_{500} \propto P_{1.4 \text{ GHz}}^{2.17 \pm 0.08}$ with total radio power (DSA+TRA) at 1.4 GHz which extends from mass $10^{13} M_{\odot}$ to more than $10^{15} M_{\odot}$. From the Figure 5, Panel 2, it is evident that our targeted objects i.e. groups are having much higher radio power than expected from observed cluster scaling and emission from groups is mainly dominated by TRA, making them detectable with the advanced radio telescopes.

4.3. Correlation among modelled radio and X-ray emissions

Shocks emerged out of mergers are responsible for heating the medium as well as acceleration of particles, increment of the turbulence, and amplification of magnetic fields in the cluster medium (e.g., Carilli & Taylor (2002); Dolag et al. (2002); Brüggén et al. (2005); Subramanian et al. (2006); Ryu et al. (2012); Paul et al. (2011)). Even though, X-ray emission takes place due to thermal bremsstrahlung of hot plasma (1-10 keV) in the IGM and radio emissions takes place due to synchrotron emission from gyrating charged particles accelerated by shocks and turbulence in the shock and turbulence amplified magnetic fields, a strong correlation has been observed to exist among them (Colafrancesco et al. 2014; Cassano et al. 2013). Since the mechanisms are different (one is thermal and other is non-thermal), the only pos-

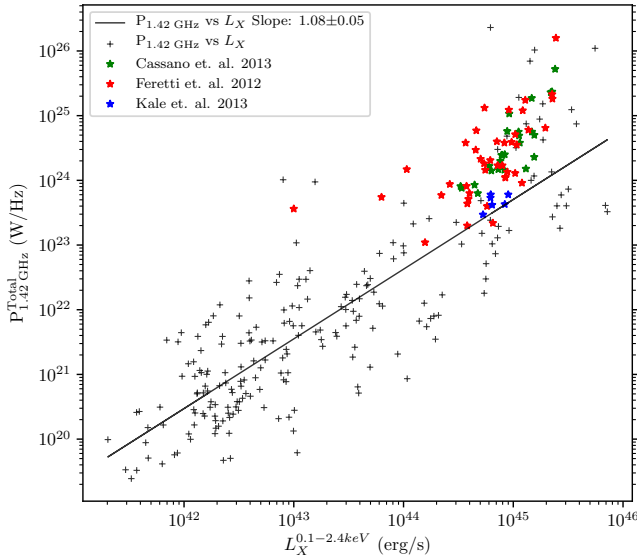


Figure 6. Over-plotted observation data on modelled X-ray luminosity vs radio power (DSA & TRA) from simulated groups and clusters.

sible explanation for this correlation can be attributed to the mergers of clusters. Since, the same merging events thermalize as well as accelerate particles that eventually emits X-ray (thermal) and radio (non-thermal), total luminosity possibly be correlated. But, the correlation of radio power at 1.4 GHz ($P_{1.4 \text{ GHz}}$) and X-ray (L_X , 0.1-2.4 keV) reported so far is for a very limited sample set and are only for large mass objects ($> 10^{14} M_\odot$), could not reveal anything about low mass ‘galaxy groups’. In Figure 6, we have plotted our modelled radio emissions (see section 3) against the modelled X-ray emission (computed using `CLOUDY` code (Ferland et al. 1998), (for detailed parameters see John et al. (2018))) from our simulated sample in the mass range 10^{13} – $10^{15} M_\odot$. The observed data from various available literature have been over-plotted in the same plot for confirming the accuracy of our model. It shows, similar to radio power mass scaling, the points that were thought to be outliers by Giovannini et al. (2011, 2009) in their $L_X - P_{1.4 \text{ GHz}}$ correlation plot, came well under our computed correlation line as shown in Figure 6. This result further validates of our model. A new correlation scale of $L_X \propto P_{1.4 \text{ GHz}}^{1.08 \pm 0.05}$ has been found in our study. Since, our model fits well to all the available observed data (see Fig. 6), it has enabled us to extend the computed correlation towards the lower mass which so far has remained unexplored.

4.4. Computing radio emissions from selected SDSS groups

Our simulated models (section 3.2, 3.3.1 and 3.3.2) compared and constraint with various available observations (as discussed in section 4.1, 4.2 and 4.3) have been implemented

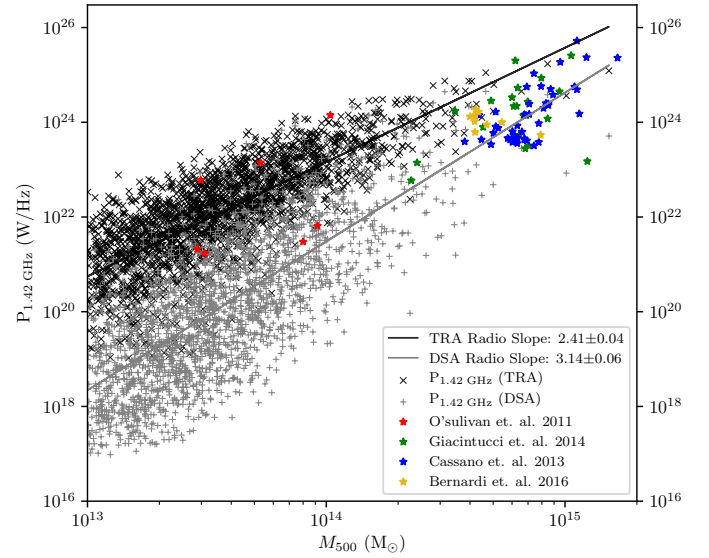


Figure 7. Modelled radio power (DSA & TRA) from SDSS groups and clusters.

to real set of objects derived from Sloan Digital Sky Survey (SDSS) data (details of the data selection in section 2.2). The most important factor for computing magnetic field and radio emission is turbulence in the medium. In our dataset of SDSS, we have data for velocity dispersion that are computed from the line-of-sight velocities of all detected member galaxies inside individual groups (Tempel et al. 2014b). Velocity dispersion is an indication of turbulence in the medium as has been discussed already (section 3.1.2). Further, SDSS dataset (Tempel et al. 2014b) contains mass, velocity dispersion etc. required parameters only at over-density 200 (i.e. r_{200}), but mostly mass and X-ray emissions are reported up to over-density 500 (i.e. r_{500}) in most of the literature. Also, radio halo emissions that usually observed is contained within the core of the structure i.e. about over-density 1000 (i.e. r_{1000}), accordingly, we have scaled required parameters using our simulations data. We have finally computed radio emissions implementing the models described in section 3.3.1 and 3.3.2.

Estimated radio emission power from the selected samples of SDSS galaxy groups and observations are over-plotted similar to Figure 5. It has been found that our computed values for SDSS data also fairly match with the observations (see Fig. 7). The only difference is the slope of TRA against mass, which is little steeper than the simulated one (see Fig. 5). For computation of expected radio emissions from SDSS groups, we had to use the averaged values which miss the possible fluctuations inside the volume explaining

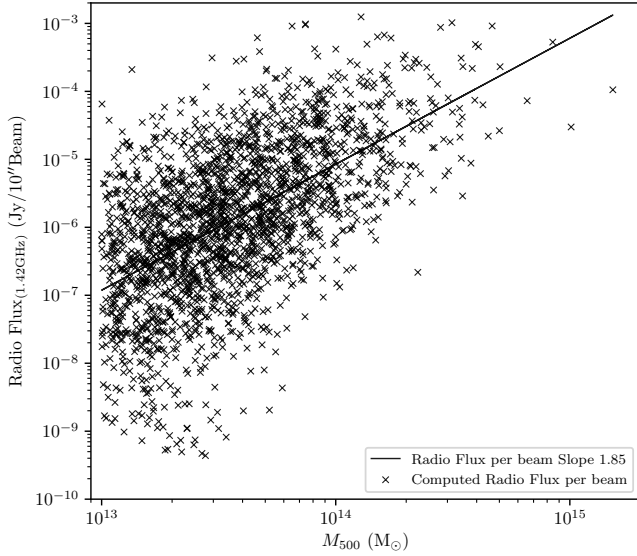


Figure 8. Total radio flux (DSA+TRA) per beam ($10''$) from our selected SDSS data set plotted vs the object mass (M_{500}).

the slight difference in slope observed compared to the simulated data.

4.5. Prospect of detection of SDSS galaxy groups

Applying our theoretical model of radio emission to the selected SDSS groups, we have estimated the 1.4 GHz flux per beam taking a beam size of ($10''$). The computed flux varies in the range of sub μJy to few 10s of μJy per beam (see Fig. 8). The radio emission produced, travel to reach the earth surface. Since, radiation goes spherically out, flux from the source goes down by a factor of L_d^2 where, L_d is the luminosity distance of each of these objects. Further, we have considered the angular extension of the radio emitting part i.e. r_{1000} of each object to compute the flux per beam. Expected 1.4 GHz flux on earth for these groups are computed in Jy/beam where $1 \text{ Jy} = 10^{-26} \text{ Watt m}^{-2}$ (beam size is $10''$) and plotted in the Figure 8. Many of the low mass objects show a promising level of fluxes that are even within the range of few existing or upgraded radio telescopes. We have further created data set of objects with expected radio flux above $100\mu\text{Jy/beam}$ (see Table will be available with the published version of the paper), in view of possible interest in astronomy community for observing them. With a $100\mu\text{Jy/beam}$ limit, we can expect to observe 75 objects i.e. about 3% of 2300 selected SDSS groups in our sample. By pushing the detection limit by 10 times i.e. to $10 \mu\text{Jy}$, we can increase our detection success rate to 21% (about 490 objects) which seems very promising with the view of upcoming telescopes such as SKA. In this context, we should mention that one of the very small mass (about $3 \times 10^{13} M_{\odot}$) object

has already been detected by us at GMRT 610 MHz and will be reported in a separate article (Paul S., et al., in preparation). Our predicted value of mean radio flux is $70\mu\text{Jy/beam}$, when observed value is about $100\mu\text{Jy/beam}$. And further detection of smaller groups (about $10^{13} M_{\odot}$) having temperature less than 1 keV will reveal the WHIMs and the missing baryons along with the nano-Gauss magnetic fields.

4.6. Limitations of this study

Our computations have been performed on a hydrodynamic set-up but, many of the parameters required for computing magnetic field and radio synchrotron emissions are purely of magnetohydrodynamic (MHD) in nature. So, for more realistic results we need to perform MHD simulations. Further, particle acceleration models are used on a set of time frozen simulation outputs, no radiation transport has been considered, and synchrotron spectral ageing has also been ignored, thus time evolution of the parameters are missing in our calculations. While implementing our simulated models to observed SDSS objects, we had to use scaling relations to compute the velocity dispersion and density. Since, SDSS parameters are available as averaged over the total volume of the objects, our computed values miss the spatial variation information. All these may lead to some amount of over or underestimation of the computed values.

5. SUMMARY AND CONCLUSION

In this study, for the first time, a comprehensive radio emission model for LSS has been presented. Our model includes synchrotron radio emission from IGM electrons accelerated by both DSA and TRA. Computed radio power in our study matched well with the available data of radio emissions at a wide range of mass and also verified with the $P_{1.4 \text{ GHz}} - L_X$ correlation plot. This is worth mentioning that our models (see section 3) are very robust and we hardly need to tweak or constrain any parameters to fit it with the observations. This enabled us to correctly extrapolate to estimate possible radio emissions from low mass objects. We report a detectable amount of radio emissions from low mass objects with the high sensitive available and upcoming radio telescopes such as uGMRT, SKA, ALMA and so on. So, the major findings from this study are as follows.

- We have modelled saturated magnetic field in groups and clusters taking very simple assumptions as described in section 3.2. Our model has been able to well reproduce the observed radial profile of coma cluster (see Fig. 4). We report a 10s of nano-Gauss to sub μG magnetic field in groups and any detection of such groups will have a significant role in constraining turbulent dynamo model in explaining the origin of cosmic magnetism.

- We have noticed that the radio halo emission observed so far in the galaxy clusters cannot be explained only with TRA model as it is usually done. We found a significant role of merger shocks even inside the r_{1000} of the clusters and we report that a combined radio power of DSA and TRA can only fit well to all the observed objects. It has also been noticed that the galaxy groups are clearly dominated by TRA radio emissions and do not fall in the current mass-radio power scaling law derived from an incomplete data set as given in [Cassano et al. \(2013\)](#); [Yuan et al. \(2015\)](#) rather, follow a flatter slope of $\alpha = 2.17 \pm 0.08$ as found in our study. Similar observation can be made about $L_X - P_{1.4\text{ GHz}}$ correlation where we found a much flatter slope of $\beta = 1.08 \pm 0.05$.
- The radio emission model devised using simulation (see section 3) has been implemented to the real objects obtained from SDSS galaxy group catalogue in our study. We found many smaller groups have the radio flux much above the detection limit of currently available telescopes. So, with a proper strategy, a considerable number of (about 3 % of the selected groups from SDSS list) of low mass objects should show up in radio soon. Indeed, we have detected radio halo

emissions from one of the very small mass (about $3 \times 10^{13} M_\odot$) SDSS object (will be reported in a separate article in Paul S., et al., in preparation). Further, with the upcoming telescopes such as SKA, we will be able to detect about 20% of the total selected SDSS groups. This also raises the hope of detection of WHIMs and can shed light on the outstanding missing baryon problem.

ACKNOWLEDGEMENTS

This project is funded by DST-INSPIRE Faculty Scheme (IFA-12/PH-44), Govt. of India. SP likes to thank Prof. Marcus Brüggen of Hamburger Sternwarte, Hamburg University for his valuable suggestions and discussions and to DESY, Hamburg for funding a visit to Hamburger Sternwarte as SFB Fellow to initiate collaborative research projects. We are thankful to The Inter-University Centre for Astronomy and Astrophysics (IUCAA) for providing the HPC facility. Computations described in this work were performed using the Enzo code developed by the Laboratory for Computational Astrophysics at the University of California in San Diego (<http://lca.ucsd.edu>), and data analysis is done with the yt-tools (<http://yt-project.org/> ([Turk et al. 2011](#))).

REFERENCES

- Baring, M. G., & Summerlin, E. J. 2009, in American Institute of Physics Conference Series, Vol. 1183, American Institute of Physics Conference Series, ed. X. Ao & G. Z. R. Burrows, 74–84
- Bernardi, G., Venturi, T., Cassano, R., et al. 2016, MNRAS, 456, 1259
- Berrier, J. C., Stewart, K. R., Bullock, J. S., et al. 2009, ApJ, 690, 1292
- Bharadwaj, V., Reiprich, T. H., Lovisari, L., & Eckmiller, H. J. 2015, A&A, 573, A75
- Bonafede, A., Feretti, L., Murgia, M., et al. 2010, A&A, 513, A30
- Brilenkov, R., Eingorn, M., & Zhuk, A. 2015, ArXiv e-prints, arXiv:1507.07234
- Brüggen, M., Bykov, A., Ryu, D., & Röttgering, H. 2012, Space Sci. Rev., 166, 187
- Brüggen, M., Ruszkowski, M., Simionescu, A., Hoeft, M., & Dalla Vecchia, C. 2005, ApJ, 631, L21
- Brunetti, G., Cappi, M., Setti, G., Feretti, L., & Harris, D. E. 2001, A&A, 372, 755
- Brunetti, G., & Lazarian, A. 2007, MNRAS, 378, 245
- Bryan, G. L., Norman, M. L., O’Shea, B. W., et al. 2014, ApJS, 211, 19
- Carilli, C. L., & Taylor, G. B. 2002, ARA&A, 40, 319
- Carnevali, P., Cavaliere, A., & Santangelo, P. 1981, ApJ, 249, 449
- Cassano, R., Brunetti, G., Setti, G., Govoni, F., & Dolag, K. 2007, MNRAS, 378, 1565
- Cassano, R., Ettori, S., Brunetti, G., et al. 2013, ApJ, 777, 141
- Cen, R., & Ostriker, J. P. 1992, ApJL, 399, L113
- Colafrancesco, S., Emritte, M. S., Mhlahlo, N., & Marchegiani, P. 2014, A&A, 566, A42
- Diaferio, A., Ramella, M., Geller, M. J., & Ferrari, A. 1993, AJ, 105, 2035
- Díaz-Giménez, E., & Mamon, G. A. 2010, MNRAS, 409, 1227
- Dolag, K., Bartelmann, M., & Lesch, H. 2002, A&A, 387, 383
- Dolag, K., Bykov, A. M., & Diaferio, A. 2008, SSRv, 134, 311
- Dolag, K., Vazza, F., Brunetti, G., & Tormen, G. 2005, MNRAS, 364, 753
- Donnert, J., & Brunetti, G. 2014, MNRAS, 443, 3564
- Drury, L. O. 1983, Reports on Progress in Physics, 46, 973
- Egan, H., O’Shea, B. W., Hallman, E., et al. 2016, ArXiv e-prints, arXiv:1601.05083
- Eilek, J. A., & Owen, F. N. 2002, ApJ, 567, 202
- Eisenstein, D. J., & Hut, P. 1998, ApJ, 498, 137
- Fang, K., & Linden, T. 2016, Journal of Cosmology and Astroparticle Physics, 2016, 004
- Feretti, L., & Giovannini, G. 2008, in Lecture Notes in Physics, Berlin Springer Verlag, Vol. 740, A Pan-Chromatic View of Clusters of Galaxies and the Large-Scale Structure, ed. M. Plionis, O. López-Cruz, & D. Hughes, 24

- Ferland, G. J., Korista, K. T., Verner, D. A., et al. 1998, *PASP*, 110, 761
- Freeland, E., & Wilcots, E. 2011, *ApJ*, 738, 145
- Giacintucci, S., Markevitch, M., Venturi, T., et al. 2014, *ApJ*, 781, 9
- Giovannini, G., Bonafede, A., Feretti, L., et al. 2009, *A&A*, 507, 1257
- Giovannini, G., Feretti, L., Girardi, M., et al. 2011, *A&A*, 530, L5
- Goldman, I. 1998, in *IAU Symposium*, Vol. 188, *The Hot Universe*, ed. K. Koyama, S. Kitamoto, & M. Itoh, 297
- Govoni, F., & Feretti, L. 2004, *International Journal of Modern Physics D*, 13, 1549
- Ha, J.-H., Ryu, D., & Kang, H. 2017, *ArXiv e-prints*, arXiv:1706.05509
- Hoefl, M., & Brüggen, M. 2007, *MNRAS*, 375, 77
- Hong, S. E., Ryu, D., Kang, H., & Cen, R. 2014, *ApJ*, 785, 133
- Iapichino, L., & Brüggen, M. 2012, *MNRAS*, 423, 2781
- Iapichino, L., Federrath, C., & Klessen, R. S. 2017, *MNRAS*, 469, 3641
- Iapichino, L., Maier, A., Schmidt, W., & Niemeyer, J. C. 2010, in *American Institute of Physics Conference Series*, Vol. 1241, *American Institute of Physics Conference Series*, ed. J.-M. Alimi & A. Fuözfa, 928–934
- John, R. S., Paul, S., Iapichino, L., Mannheim, K., & Kumar, H. 2018, *ArXiv e-prints*, arXiv:1803.04445
- Jones, B. J., Martínez, V. J., Saar, E., & Trimble, V. 2004, *Reviews of Modern Physics*, 76, 1211
- Jubelgas, M., Springel, V., Enßlin, T., & Pfrommer, C. 2008, *A&A*, 481, 33
- Kale, R., Dwarakanath, K. S., Vir Lal, D., et al. 2016, *Journal of Astrophysics and Astronomy*, 37, 31
- Kent, S. M., & Gunn, J. E. 1982, *AJ*, 87, 945
- Komatsu, E., Dunkley, J., Nolte, M. R., et al. 2009, *ApJS*, 180, 330
- Kubo, J. M., Stebbins, A., Annis, J., et al. 2007, *ApJ*, 671, 1466
- Lietzen, H., Tempel, E., Heinämäki, P., et al. 2012, *A&A*, 545, A104
- Lighthill, M. J. 1952, *Proceedings of the Royal Society of London Series A*, 211, 564
- Longair, M. S. 2011, *High Energy Astrophysics* (Cambridge University Press)
- Lovisari, L., Reiprich, T. H., & Schellenberger, G. 2015, *A&A*, 573, A118
- Machado, R. E. G., & Lima Neto, G. B. 2013, *MNRAS*, 430, 3249
- McCarthy, I. G., Schaye, J., Ponman, T. J., et al. 2010, *MNRAS*, 406, 822
- Miniati, F., & Beresnyak, A. 2015, *Nature*, 523, 59
- Miniati, F., Ryu, D., Kang, H., et al. 2000, *ApJ*, 542, 608
- Moss, C. 2006, *MNRAS*, 373, 167
- O’Shea, B. W., Bryan, G., Bordner, J., et al. 2004, *ArXiv Astrophysics e-prints*, astro-ph/0403044
- O’Sullivan, E., Combes, F., Hamer, S., et al. 2015, *A&A*, 573, A111
- O’Sullivan, E., Giacintucci, S., David, L. P., et al. 2011, *ApJ*, 735, 11
- Paul, S. 2012, *Journal of Physics: Conference Series*, 405, 012026
- Paul, S., Datta, A., & Intema, H. T. 2014, in *Astronomical Society of India Conference Series*, Vol. 13, *Astronomical Society of India Conference Series*, 187–191
- Paul, S., Gupta, P., John, R. S., & Punjabi, V. 2015, in *The Many Facets of Extragalactic Radio Surveys: Towards New Scientific Challenges*, 65
- Paul, S., Iapichino, L., Miniati, F., Bagchi, J., & Mannheim, K. 2011, *ApJ*, 726, 17
- Paul, S., John, R. S., Gupta, P., & Kumar, H. 2017, *MNRAS*, 471, 2
- Perez, J., Tissera, P., Padilla, N., Alonso, M. S., & Lambas, D. G. 2009, *MNRAS*, 399, 1157
- Pimbblet, K. A. 2011, *MNRAS*, 411, 2637
- Pratt, G. W., Croston, J. H., Arnaud, M., & Böhringer, H. 2009, *A&A*, 498, 361
- Rasmussen, J., Ponman, T. J., Mulchaey, J. S., Miles, T. A., & Raychaudhury, S. 2006, *MNRAS*, 373, 653
- Rephaeli, Y., & Persic, M. 2015, *ApJ*, 805, 111
- Rincon, F., Califano, F., Schekochihin, A. A., & Valentini, F. 2016, *Proceedings of the National Academy of Science*, 113, 3950
- Roettiger, K., Burns, J. O., & Stone, J. M. 1999, *ApJ*, 518, 603
- Ryu, D., Kang, H., Cho, J., & Das, S. 2008, *Science*, 320, 909
- Ryu, D., Schleicher, D. R. G., Treumann, R. A., Tsagas, C. G., & Widrow, L. M. 2012, *SSRv*, 166, 1
- Saha, M. N. 1920, *The London, Edinburgh, and Dublin Philosophical Magazine and Journal of Science*, 40, 472
- Sarazin, C. L. 2002, in *Astrophysics and Space Science Library*, Vol. 272, *Merging Processes in Galaxy Clusters*, ed. L. Feretti, I. M. Gioia, & G. Giovannini, 1–38
- Sarazin, C. L., & White, III, R. E. 1987, *ApJ*, 320, 32
- Skillman, S. W., O’Shea, B. W., Hallman, E. J., Burns, J. O., & Norman, M. L. 2008, *ApJ*, 689, 1063
- Springel, V., Frenk, C. S., & White, S. D. M. 2006, *Nature*, 440, 1137
- Stein, R. 1974, *A&A*, 35, 17
- Struck, C. 2011, *Galaxy Collisions* (Springer)
- Subramanian, K. 1998, *MNRAS*, 294, 718
- Subramanian, K., Shukurov, A., & Haugen, N. E. L. 2006, *MNRAS*, 366, 1437
- Tempel, E., Kipper, R., Saar, E., et al. 2014a, *A&A*, 572, A8
- Tempel, E., Tamm, A., Gramann, M., et al. 2014b, *A&A*, 566, A1
- Tully, R. B. 1987, *ApJ*, 321, 280
- Turk, M. J., Smith, B. D., Oishi, J. S., et al. 2011, *ApJS*, 192, 9
- Vajgel, B., Jones, C., Lopes, P. A. A., et al. 2014, *ArXiv e-prints*, arXiv:1409.6822

- van Weeren, R. J., Brüggen, M., Rottgering, H. J. A., & Hoeft, M. 2011, *Monthly Notices of the Royal Astronomical Society*, 418, 230
- Vazza, F., Dolag, K., Ryu, D., et al. 2011, *MNRAS*, 418, 960
- Vazza, F., Jones, T. W., Brüggen, M., et al. 2017, *MNRAS*, 464, 210
- Wilman, D. J., Balogh, M. L., Bower, R. G., et al. 2005, *MNRAS*, 358, 71
- Xu, H., Li, H., Collins, D. C., Li, S., & Norman, M. L. 2009, *ApJL*, 698, L14
- Yuan, Z. S., Han, J. L., & Wen, Z. L. 2015, *ApJ*, 813, 77
- Zhang, Y., Yang, X., Wang, H., et al. 2013, *ApJ*, 779, 160
- Zhu, Y., & Antonia, R. A. 1997, *Applied Scientific Research*, 57, 337

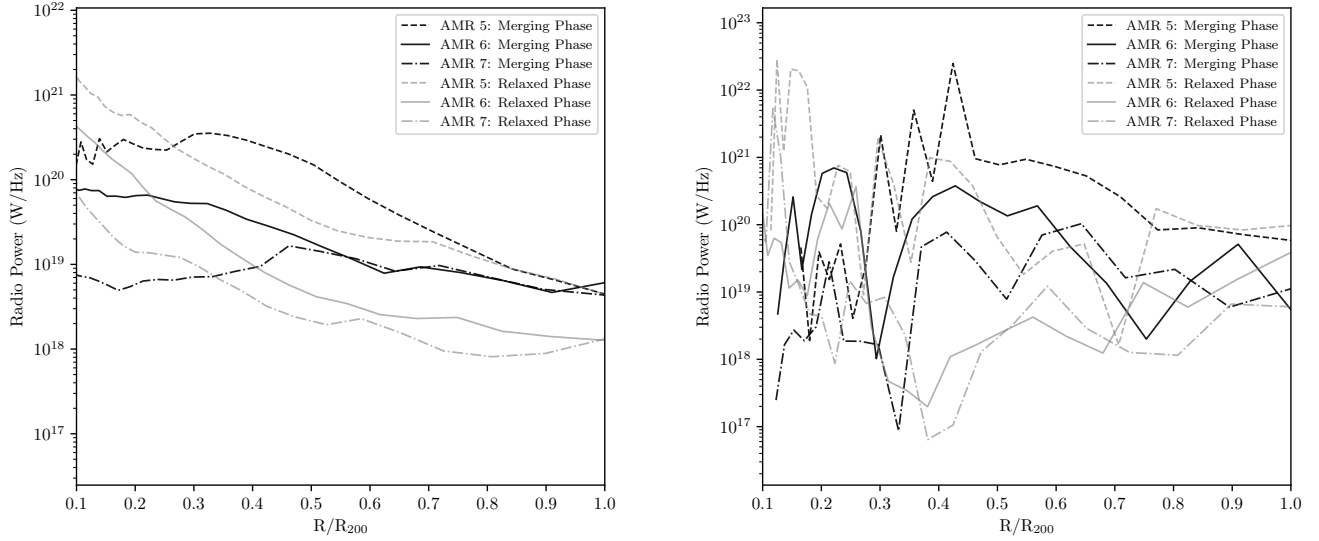


Figure 9. Computed radio power (Panel 1 is TRA and Panel 2 is DSA) have been plotted against normalised radius (normalised to r_{200}) for merging and relaxed states, of a galaxy cluster with final mass about $10^{15} M_{\odot}$ and for three resolutions namely LowRES, RefRES and HighRES (as indicated in the legend respectively)

APPENDIX

A. RESOLUTION STUDY

With the cosmological and simulation parameters described in section 2.1, we have simulated realisations with 6 levels of total (uni-grid + AMR) refinement leading to a resolution of about 30 kpc i.e. the RefRES. For the resolution study, apart from this RefRES, we have simulated two other sets of data with a lower resolution (‘LowRES’ hereafter) reaching ~ 60 kpc with total 5 AMR and a higher resolution with total 7 AMR (‘HighRES’ hereafter) ~ 15 kpc by keeping the other parameters same. We have also produced two simulations having two different root Grid resolutions besides the ‘RefRES’. High resolution root grid simulation is done with 128^3 and is named as ‘RootHighRES’ and low resolution one is with 32^3 root grids and called as ‘RootLowRES’. But, in these last two simulations, the final resolution is same as the RefRES i.e. about 30 kpc at the highest resolution level.

In Figure 9, radial variations of radio power due to TRA (Panel 1) and DSA (Panel 2) respectively have been plotted for merging (Black) and relaxed phase (Grey) of the cluster CL_2 . It can be noticed that RefRES simulation is almost same as the HighRES resolution with some deviation in the central region of the cluster, though, LowRES data are far away. Radio luminosity varies smoothly in case of TRA electrons as this comes from a bulk property of the cluster whereas fluctuations are more in case of DSA as it has resulted from shocks which is a transient effect which is strongly dependent on resolution.

Another two sets of data with different root grid resolution namely RootLowRES and RootHighRES have been simulated. We have further chosen appropriate merging and non-merging states and plotted the radio emissions again from both TRA and DSA electrons. Though we observe a reasonable convergence during non-merging phase, merging phases show a greater deviation at least in some part of the objects where shock has propagated (see Fig. 10, Panel 1). Again, the discrepancy can be attributed to the resolution sensitivity of dynamical effects but the total emissions from the whole object seems not changing much. This indicates that though there could be a little time shift in the parameters but has no gross deviation from computed magnitude of the parameters when measured by compensating the time.

These results thus show that our simulated parameters are almost converging with the resolution that we took as the reference set of simulations i.e. about 30 kpc with 6 levels of refinement. For further details of resolution study of our data sets, we suggest to go through Paul et al. (2017); John et al. (2018).

B. TABLE OF OBJECTS WITH PREDICTED RADIO FLUX OF $50 \mu\text{JY}/\text{BEAM}$

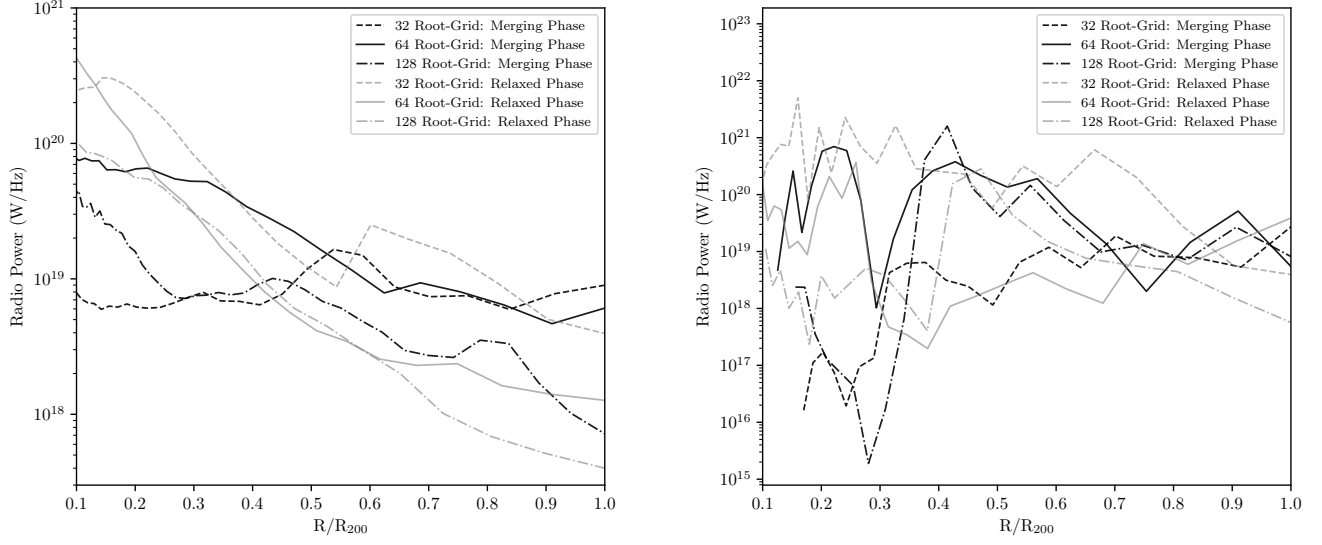


Figure 10. Plot of radial (normalised radius, as in Fig. 9) radio power (Panel 1 is TRA and Panel 2 is DSA) for the same dynamical phases for different root grid resolution simulations with the same final resolution of about 30 kpc.